

Geophysical Research Letters[®]

RESEARCH LETTER

10.1029/2021GL095839

Key Points:

- Nightglow emissions excited by photoelectrons originating in the magnetically conjugate hemisphere are observed by the ICON mission
- Conjugate photoelectron energy spectra are derived for the first time using global scale far-ultraviolet and radio-occultation observations
- Comparison of estimated photoelectron fluxes with measurements on a rocket flight shows consistent characteristics at all altitudes

Correspondence to:






J. M. Urco,
mcordero@illinois.edu

Citation:

Urco, J. M., Kamalabadi, F., Kamaci, U., Harding, B. J., Frey, H. U., Mende, S. B., et al. (2021). Conjugate photoelectron energy spectra derived from coincident FUV and radio measurements. *Geophysical Research Letters*, 48, e2021GL095839. <https://doi.org/10.1029/2021GL095839>

Received 1 SEP 2021
Accepted 20 NOV 2021

Conjugate Photoelectron Energy Spectra Derived From Coincident FUV and Radio Measurements

J. M. Urco^{1,2} , F. Kamalabadi¹, U. Kamaci¹, B. J. Harding³ , H. U. Frey³ , S. B. Mende³ , J. D. Huba⁴, S. L. England⁵ , and T. J. Immel³

¹Department of Electrical and Computer Engineering and Coordinated Science Laboratory, University of Illinois at Urbana-Champaign, Urbana, IL, USA, ²Leibniz-Institute for Atmospheric Physics, University of Rostock, Kuehlungsborn, Germany, ³Space Sciences Laboratory, University of California-Berkeley, Berkeley, CA, USA, ⁴Syntek Technologies, Fairfax, VA, USA, ⁵Virginia Polytechnic and State University, Blacksburg, VA, USA

Abstract We present a method for estimating incident photoelectrons' energy spectra as a function of altitude by combining global scale far-ultraviolet (FUV) and radio-occultation (RO) measurements. This characterization provides timely insights important for accurate interpretation of ionospheric parameters inferred from the recently launched Ionospheric Connection Explorer (ICON) observations. Quantification of photoelectron impact is enabled by the fact that conjugate photoelectrons (CPEs) directly affect FUV airglow emissions but not RO measurements. We demonstrate a technique for estimation of photoelectron fluxes and their spectra by combining coincident ICON and COSMIC2 measurements and show that a significant fraction of ICON-FUV measurements is affected by CPEs during the winter solstice. A comparison of estimated photoelectron fluxes with measured photoelectron spectra is used to gain further insights into the estimation method and reveals consistent values within 10–60 eV.

Plain Language Summary The impact of solar radiation on the atmosphere produces highly energetic electrons, which travel freely along the magnetic Earth's field lines from one hemisphere to the other. When these electrons flow from the sunlit side into the nightside hemisphere, they interact with the neutral species and produce noticeable effects in the ionosphere such as an increase in electron temperature and enhancement of airglow emissions. This study presents a method to quantify the amount of precipitating electrons and their energy on a global scale using two recent satellite missions, ICON and COSMIC2. Our results demonstrate that coincident far-ultraviolet (ICON) and radio-occultation (COSMIC2) measurements from space are valuable resources to study precipitating electrons in the ionosphere and their impact on inferring ionospheric plasma parameters.

1. Introduction

Photoionization of the neutral atmospheric species by solar radiation and X-rays produces highly energetic electrons in the ionosphere, also known as photoelectrons. Conjugate photoelectrons (CPEs) refer to those PE that travel along the magnetic field lines from one hemisphere to the other and lose their energy through inelastic collisions with neutral particles and ambient electrons in the local region. Such interactions result in elevation of ambient electron's temperature (Duboin et al., 1968), additional electron production (Swartz, 1972), and enhancement of airglow emissions (Cole, 1965; Duboin et al., 1968; Fontheim et al., 1968; Hanson, 1963).

Although CPEs' effects are present during day and night, their impacts are more significant at night, when and where the local point is in darkness and its magnetically conjugate point is not. Evidence of an increase in electron temperature by more than 100% at pre-dawn caused by CPE impact has been reported using in-situ satellite measurements (Narasinga Rao & Maier, 1970), and incoherent scatter radar (ISR) measurements (Carlson, 1966, 1968; Evans, 1967). Moreover, pre-dawn airglow enhancements at visual wavelengths have been reported by various authors (Bennett, 1969; Carman et al., 1969; Christensen, 1975; Cogger & Shepherd, 1969; Smith, 1969). At far-ultraviolet (FUV) wavelengths, Meier (1971) reported the first observations of airglow enhancement at pre-dawn using OGO-4. More recently, Solomon et al. (2020) and Kil et al. (2020) have reported pre-dawn airglow enhancements observed by GOLD (Eastes et al., 2008, 2017) and SSUSI (Paxton et al., 2017, and references therein), respectively. In both cases, regions affected by CPEs show one order of magnitude brighter airglow emissions than those not affected.

The first direct measurements of CPE fluxes date back to Peterson et al. (1977) using the Atmosphere Explorer C, and to Shepherd et al. (1978) and Mukai et al. (1979) using sounding rockets. They found CPEs can travel along the magnetic field lines from one hemisphere to the other without significant degradation. Furthermore, they reported that more than 65% of the 630 nm airglow emissions were produced by direct impact of photoelectrons with atomic oxygen. Another substantial amount of photoelectron measurements from 1996 to 2009 at 3,500 km altitude is available from the FAST satellite (Pfaff et al., 2001). Using FAST data, Richards and Peterson (2008) found that about 60% of the precipitating energy flux is backscattered to the conjugate hemisphere. Despite the existing observations, the resulting data do not provide sufficient spatial and temporal coverage to specify photoelectron fluxes for all geophysical, temporal, and altitudinal conditions. Consequently, parameterized models have been developed and are generally used to obtain photoelectron fluxes.

Nagy and Banks (1970) performed initial photoelectron generation, transport, and impact calculations. Since then, various methods have been developed to model photoelectron transport in the ionosphere such as FLIP (Richards & Torr, 1990), SUPIM (Bailey & Balan, 1996), GLOW (Solomon, 2017), and SAMI2-PE (Varney et al., 2012). Among all these numerical first-principle calculations, the multi-stream photoelectron transport model implemented in SAMI2-PE is one of the most comprehensive and was able to closely reproduce the electron temperature and density observed by Jicamarca at all local times. Nevertheless, the high fidelity achieved by multi-stream electron transport comes with a considerable computational price, and it is sensitive to the selected pitch angle resolution. Other faster method such as the two-stream electron transport implemented in GLOW has demonstrated to be good at reproducing twilight airglow emissions observed by GOLD at latitudes lower than 60° (Solomon et al., 2020), although some discrepancies observed at mid and high latitudes were associated with the reduced number of pitch angles used, and other neglected terms such as scattering losses or meridional transport.

Besides models, several techniques have been proposed to estimate photoelectron fluxes from measurements. Early attempts to infer photoelectron fluxes from simultaneous measurements of the OI lines and the N₂ band, and from ISR measurements using the continuity equation were described by M. H. Rees and Luckey (1974) and Semeter and Kamalabadi (2005), respectively. Although the ISR-based problem has the advantage of possessing more degrees of freedom and the capability to retrieve altitude information compared to that of optical measurements, it is still sensitive to the pitch angle distribution assumed, and its estimates are confined to a specific geographic location.

This study develops a method for estimating photoelectron energy fluxes as a function of altitude on a global scale from combined FUV and radio-occultation (RO) measurements. The main challenge in interpreting FUV observations independently is to separate volume emissions due to radiative recombination (RR) and mutual neutralization (MN) from that due to photoelectron impact. We employ RO measurements to perform full RR and MN calculations and use these results to isolate the photoelectron contribution from FUV measurements. Once the photoelectron contribution is isolated, it is used to estimate photoelectron fluxes.

In contrast to available global photoelectron observations which do not provide altitude information (Pfaff et al., 2001), or to ISR methods which are confined to one geographic location (Semeter & Kamalabadi, 2005), our technique enables, for the first time, quantification of photoelectron fluxes globally as a function of altitude and energy. This new capability provides further insight into the energetics of the thermosphere/ionosphere and can complement models to explain observations that cannot be reproduced precisely.

2. FUV and RO Measurements

2.1. ICON: FUV Measurements

The Ionospheric Connection Explorer (ICON) is a NASA mission launched in October 2019 into a 27° inclination, 598 km altitude near-circular orbit and equipped with four scientific instruments. ICON is dedicated to making continuous observations of the neutral atmospheric drivers and the resulting ionospheric responses (Immel et al., 2018).

One of the ICON's payloads is the FUV instrument, which was designed to provide disk and limb-scan images during day and nighttime (Mende et al., 2017). During nighttime, the FUV instrument images the limb altitude profile in the shortwave band at 135.6 nm. This band is sensitive to the OI 135.6 nm emission and also to LBH

(2,0), (3,0), (4,0) and (5,2) bands in its passband. In this work, we only consider the influence from OI 135.6 nm, the dominant source.

To infer O⁺ density profiles, which in the nighttime ionosphere is approximately equal to the electron density, the ICON's field of view is divided into six vertical stripes, where each stripe has a horizontal (along track) and vertical (cross-track) resolution of 128 and 4 km at 155 km altitude, respectively.

The operational forward model to infer electron density from limb viewing integrated OI 135.6 nm emissions includes the two primary mechanisms, namely, RR and MN (Kamalabadi et al., 2018; Qin et al., 2015). A third source which is not usually considered is airglow emissions due to CPE impact, which at some times and particular locations is more important than the first two. Since the ICON's algorithm (Kamalabadi et al., 2018) did not consider the CPE source, we use volume emission rates (VERs) estimated from ICON-FUV images and combine them with COSMIC2 occultations to isolate the CPE contribution.

2.2. COSMIC2: RO Measurements

The Constellation Observing System for Meteorology, Ionosphere and Climate-2 (COSMIC2) is an international Taiwan-US mission consisting of six low-Earth orbiting (LEO) satellites launched in 2019 into a 24° inclination, 520 km circular orbit (Anthes & Schreiner, 2019; Schreiner et al., 2020). The primary payload of each LEO satellite is a Tri-Global Navigation Satellite System (GNSS) RO receiver, which has GPS, GALILEO, and GLONASS tracking capability (Tien et al., 2012). GNSS satellites orbit Earth at 20,000 km and broadcast signals at two different L-band frequencies. The RO receiver measures the phase and amplitude of GNSS radio signals as GNSS satellites are occulted by the Earth's ionosphere. Under the assumption of straight-line propagation of GNSS signals, the total electron content (TEC) along the LEO-GPS link can be calculated from the phase difference of two received L-band signals (e.g., Kuo et al., 2004; Schreiner et al., 2007; Schreiner et al., 1999; Yue et al., 2013, and references therein).

Furthermore, by assuming a spherically symmetrical atmosphere, the altitudinal electron density profile is derived through recursive inversion of slant TEC (e.g., Lei et al., 2007; Schreiner et al., 1999). COSMIC2 uses the so-called onion peeling method that calculates electron density of discrete layers below the LEO altitude starting from the uppermost altitude, on both the ascending and descending parts (Syndergaard et al., 2005). Since the LEO satellites move as they collect the GNSS signals, the LEO-GNSS link's geographical location at the top and the bottom altitude might differ by several hundred kilometers (up to 1,500 km). Therefore, horizontal ionospheric gradients may significantly affect the retrievals. Although the symmetry assumption is not always fulfilled, COSMIC2 satellites are expected to provide 5,000 vertical density profiles per day with a F peak-density and peak-height within 15% and 20 km accuracy, respectively (W. S. Schreiner et al., 2020; Yue et al., 2014).

3. Excitation of OI 135.6 nm Nightglow Emissions by Conjugate Photoelectrons

The two primary production mechanisms of OI 135.6 nm emissions in the nighttime ionosphere are RR of electrons with O⁺, and MN of O⁺ with O⁻ (Meier, 1991, and references therein). In addition, there are some times and regions when and where the magnetically conjugate point is sunlit and the local point is not. In those cases, photoelectrons produced by photoionization in the sunlit hemisphere are transported along the magnetic field lines to the other hemisphere and excite the neutral atoms in the nightside, producing additional airglow emissions.

CPE features are mostly visible during the winter solstice when the sun set/rises later/earlier in the conjugate point than in the local point. During equinox the difference between conjugate and local sunrise/sunset decreases, therefore, reducing the period and areas affected by CPEs. Figure 1a shows disk images at 135.6 nm obtained from GOLD on 6 January 2020 at 07:21 UTC similar to those shown by Solomon et al. (2020). Note that airglow emissions in the dayside are at least two orders of magnitude brighter than the nightside's. Interestingly, there is an area of faint airglow emissions in the nightside near the terminator whose morphology matches perfectly with the magnetically conjugate trace of the day/night side terminator, suggesting that these faint emissions are most likely produced by CPE impact. The northern hemisphere aurora is also visible in the GOLD data over the Hudson Bay.

VERs at the F-peak height (~250 km) estimated from ICON are shown in Figure 1b. The VERs are estimates averaged for all January 2020 around 07:30 UTC ±30 min. Although the twilight airglow morphology changes

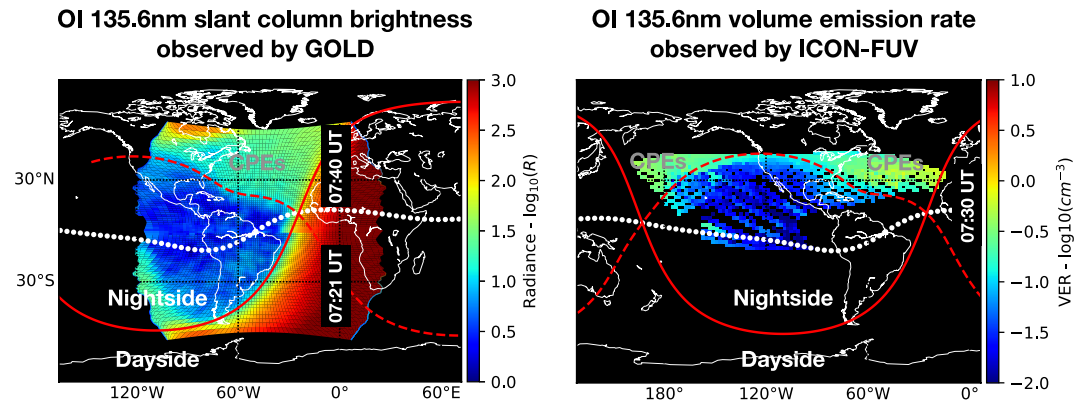


Figure 1. Airglow emissions at 135.6 nm observed by GOLD (left) and by ICON-FUV (right). Two GOLD image sequences of the OI 135.6 nm emission on January 6, 2020 at 07:21UT and 07:40UT are shown. VERs by ICON are one-hour average values around 07:30UT during January 2020. The magnetic equator (white dots), the nighttime terminator at 300 km altitude (solid red line), and its magnetically conjugate trace (dashed red line) are shown for reference. On the nightside, faint airglow emissions (green-yellowish areas) evidence conjugate photoelectron excitation.

slowly with time, the main pattern remains and it is similar to the one observed by GOLD. Besides the airglow emission at pre-dawn, there is a faint nightglow region near the evening terminator, which matches with the conjugate trace of the evening terminator. Airglow emissions due to photoelectron impact, MN, and RR are present at post-dusk and pre-dawn. Therefore, contributions to the OI 135.6 nm airglow from RR, MN, and CPE impact need to be isolated to accurately interpret FUV observations at those times.

4. Retrieving Photoelectron Energy Spectra From FUV and RO Measurements

To estimate the photoelectron energy spectra, we first isolate emission generated through photoelectron impact from the total airglow emissions. FUV instruments such as ICON-FUV or GUVI (Christensen et al., 1994) that measure limb viewing integrated airglow emissions allow inference of the source VER of OI 135.6 nm as a function of altitude (Comberiate et al., 2007; Kamalabadi et al., 2018; Qin et al., 2015). When these emissions are affected by CPEs, contributions due to RR and MN cannot be readily isolated from that due to photoelectron impact.

The source VER ε_0 of the 135.6 nm line can be calculated by

$$\varepsilon_0(h) = \varepsilon_{rr}(h) + \varepsilon_{mn}(h) + \varepsilon_{pe}(h), \quad (1)$$

where ε_{rr} , ε_{mn} , ε_{pe} are the isotropic volume emissivities due to RR, MN, and CPE impact at an altitude h , respectively. The first term ε_{rr} is a function of electron density N_e and atomic oxygen ion density [O+] (Hanson, 1969). Likewise, ε_{mn} is a function of N_e , [O+], and atomic oxygen density [O] (Hanson, 1970; Knudsen, 1970; Tinsley et al., 1973). In the F region ionosphere O+ is the dominant ion species and [O+] can be considered approximately equal to N_e . Moreover, assuming that [O] is known, for example, from the NRL-MSISE00 model (Picone et al., 2002), ε_{rr} and ε_{mn} can be expressed as a function of one unknown only, N_e (Kamalabadi et al., 2018; Qin et al., 2015). This simplification allows full RR and MN calculations from electron density measurements obtained by ionosondes, ISRs, or RO measurements.

When coincident FUV and RO measurements exist, ε_0 can be measured from FUV instruments onboard satellites, and ε_{rr} and ε_{mn} can be inferred from RO measurements. Therefore, an estimate of the volume excitation rate $\tilde{\varepsilon}_{pe}$ can be calculated using Equation 1. The vast quantity of density profiles available from ICON and COSMIC2 permit estimations of $\tilde{\varepsilon}_{pe}$ on a global scale.

4.1. Forward Model

As discussed by Meier (1991), airglow emissions at 135.6 nm from photoelectron impact occur primarily through excitation of ground-state O(³S) atoms. The rate of excitation ε_{pe} can be expressed as a function of the photoelectron flux by

$$\varepsilon_{pe}(h) = [O](h) \int_{E_{\min}}^{E_{\max}} \phi(h, E) \sigma(E) dE, \quad (2)$$

where $\sigma(E)$ (cm^{-2}) is the electron impact excitation cross section, $\phi(h, E)$ ($cm^{-2}s^{-1} eV^{-1}$) is the photoelectron flux at altitude h and energy E , and E_{\min} is the threshold energy for excitation. Typical values for E_{\min} and E_{\max} are 5 and 100 eV, respectively, since out of this range the excitation cross-sections for OI 135.6 nm are negligible. The model cross-sections are available from (Meier, 1991) and the atomic oxygen density [O] from the NRL-MSISE00 model (Picone et al., 2002). Thus, ε_{pe} can be expressed as a function of the photoelectron flux only. Despite this simplification, the problem in Equation 2 is ill-posed and cannot be solved without additional regularization terms.

As discussed by Kaeppler et al. (2020), there are three methods to model photoelectron transport from the magnetosphere to the ionosphere and that can be incorporated in our forward model: (a) empirically derived methods from laboratory experiments (e.g., M. Rees, 1963; Sergienko & Ivanov, 1993; Stolarski, 1968), (b) numerical solutions to transport equations (e.g., Banks & Nagy, 1970; Nagy & Banks, 1970; Strickland et al., 1989), and (c) Monte Carlo methods (e.g., Solomon, 2001, and references therein).

For simplicity we adopt the approach described by Stolarski (1968) to determine the average loss of an electron as it traverses the atmosphere. First, we divided the precipitating photoelectron spectra in K intervals and evaluate each interval separately. Second, we consider that electrons in each interval lose part of their energy based on the depth of penetration $z(h_i, E_k) = s(h_i)/R(E_k)$, which can be expressed as

$$\Delta E_{ik} = \Delta E(h_i, E_k) = E_k \int_0^z \lambda(E_k, z') dz', \quad (3)$$

where ΔE_{ik} is the energy loss of an electron with initial energy E_k when it reaches an altitude h_i , $s(h) = \int_h^{h_{top}} \rho(h') dh'$ is the scattering depth as a function of altitude ($g cm^{-2}$), $\rho(h)$ is the atmospheric mass density given by the NRL-MSISE-00 model ($g cm^{-3}$), $R(E)$ is the experimentally derived average range of an electron in air ($g cm^{-2}$), and $\lambda(E, z)$ is the experimentally derived fraction of energy lost per fraction of mass distance traveled (dimensionless). With this approach the relevant physics is included implicitly in the experiments and the residual photoelectron flux at altitude h_i and energy bin E_j can be conveniently expressed as a function of the precipitating electron beam at the top of the atmosphere $\phi(E_k) = \phi(h_{top}, E_k)$ as

$$\phi(h_i, E_j) = \sum_k \delta(E_k - \Delta E_{ik} - E_j) (1 - A(E_k)) \phi(E_k), \quad (4)$$

$$= \sum_k M_{ijk} (1 - A(E_k)) \phi(E_k), \quad (5)$$

where δ is the Dirac delta function, and $A(E_k)$ is the experimentally derived albedo-flux which accounts for the electron flux reflected by the atmosphere (backscattered flux). M is a sparse matrix whose elements are only unity when $E_j = E_k - \Delta E_{ik}$.

Equation 5 considers that each incident (non-backscattered) electron has lost a fraction of its energy and thus slowed down as it penetrates the atmosphere. This is a more realistic assumption than considering that a small fraction of electrons have been completely absorbed while the rest continued unchanged in energy (Stolarski, 1968). Although this assumption might not be satisfied completely at all altitudes, no error is propagated down in altitude since the residual flux at each altitude is calculated directly from the precipitating flux at the top of the atmosphere.

The residual energy E_j does not necessarily coincide with the selected energy intervals. To avoid spurious structures in the spectrum, the residual photoelectron flux is spread over the two energy bins adjacent to E_j based on the distance between E_j and the energy bins, that is, $0 < M_{ijk} < 1$.

Using Equation 5, Equation 2 can be expressed as a function of the incident photoelectron flux at, for example, $h_{top} = 500$ km altitude

$$q(h_i) = \frac{\epsilon_{pe}(h_i)}{[O](h_i)} = \sum_k M'_{ik} (1 - A(E_k)) \phi(E_k), \quad (6)$$

where $M'_{ik} = \sum_j M_{ijk} \sigma_j \Delta e_j$, and Δe_j is the energy step.

A similar approach based on the measurements of M. Rees (1963) was incorporated into the ISR inverse problem to estimate photoelectron fluxes by Semeter and Kamalabadi (2005). In the present study, the energy-dependent values λ , R , and A of Sergienko and Ivanov (1993) for an isotropic electron beam were chosen as they are more accurate than those of M. Rees (1963), especially at low energies where λ shows a strong energy dependence.

4.2. Inversion Method

Equation 6 is a typical inverse problem and can be solved by various constrained optimization methods. In this work, we employ the regularized weighted least squares (RWLS) method (Zhang et al., 2014). The first derivative operator was selected as regularizer and the regularization parameter was chosen via cross-validation techniques (Molinaro et al., 2005). To avoid numerical problems due to the very small values in Equation 6, the left- and right-hand side of Equation 6 were multiplied by 10^{10} . Considering this factor, the regularization parameter varies between 10^{-5} and 2×10^{-5} .

Semeter and Kamalabadi (2005) employed a maximum entropy method (MEM) to solve a similar problem. Simon-Wedlund et al. (2013) revisited this method and showed that both the multiplicative algebraic reconstruction technique (MART) and MEM are suitable for solving the ISR problem. The advantage of these methods over RWLS is that they allow large variations in the resulting spectra. In our case, even using MEM or MART the resulting spectra were still smooth. This is caused by the smooth profiles provided by both ICON and COSMIC2.

5. Experimental Results

We now present results of CPE energy spectra inversion from coincident ICON and COSMIC2 observations in the nighttime ionosphere. Figure 2a shows the ICON satellite's location, the ICON-FUV's line of sight, and the ionospheric pierce point of ICON and COSMIC2 on 04/01/2020 at 11:09:19 UTC. The spatial separation between pierce points is less than 4° in both latitude and longitude, and less than 15 min in time (criteria for coincident observations). The ICON-FUV's line of sight and its conjugate trace are included for determining what percent of the latter is sunlit. When the conjugate trace is in the darkness, VERs estimated from ICON and COSMIC2 are expected to be similar. However, when the conjugate trace is completely sunlit, the VER observed by ICON is up to one order of magnitude higher than that of COSMIC2.

Figure 2b shows the source VER observed by ICON, the VER due to RR + MN calculated from COSMIC2 observations, and the volume excitation rate due to CPE impact calculated from Equation 1 for the selected example. Recent comparisons of NmF2 from ICON and COSMIC2 (Wautelet et al., 2021), and internal comparisons of electron density profiles from ICON and ISR at Millstone Hill suggest that the ICON-FUV measurements require a calibration factor between 0.5 and 0.6. Therefore, we scaled the ICON-FUV VERs by a factor of 0.5 to reduce the mean NmF2 difference between coincident ICON/COSMIC2 observations to zero. The calibrated ICON values are used along this study.

Figure 2c shows the geographical distribution of coincident measurements by ICON and COSMIC2 during January/February 2020. About 35% of ICON-FUV data in the nighttime showed evidence of CPEs during the winter solstice. Figure 2d shows the ICON and COSMIC2 VER difference as a function of the percent of the conjugate trace in sunlit conditions, hereafter the "sunlit conjugate". Figure 2d shows an explicit dependency between the VER difference and the sunlit conjugate. Note that the mean V/IER difference between ICON/COSMIC2 is zero

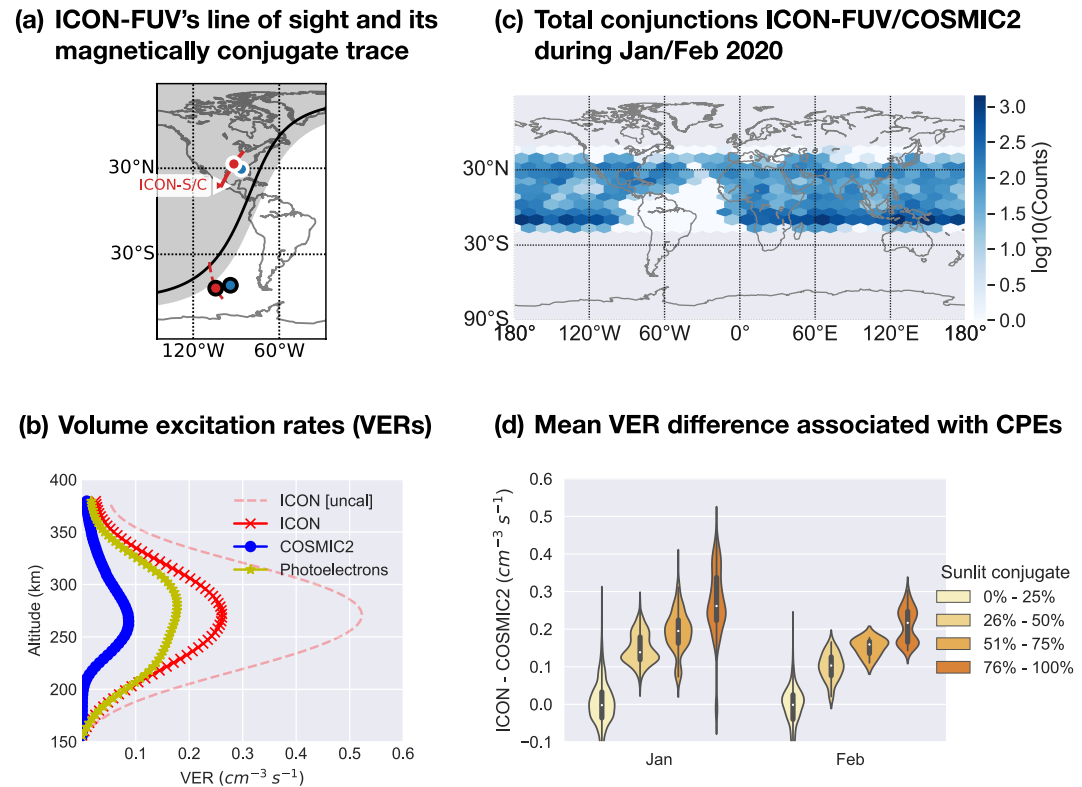


Figure 2. Coincident volume emission rate (VER) measurements by ICON and COSMIC2. (a) ICON (red circle) and COSMIC2 (blue circle) satellite's location on 04/01/2020 at 11:09:19 UTC. Far-ultraviolet (FUV's) line of sight at the peak height (solid red line) and its magnetically conjugate trace (dashed red line) in the northern and southern hemisphere, respectively. Besides the night/day side at the sea level, the terminator at 300 km is indicated by a solid black line. (b) Uncalibrated and calibrated VERs measured by ICON-FUV (dashed and solid red lines, respectively), VER due to RR and MN inferred from COSMIC2 (blue), and VER difference associated with CPE impact (yellow) for the same time as (a). (c) Geographical distribution of total coincidences ICON/COSMIC2 during January/February 2020 (d) Mean VER difference between coincident ICON/COSMIC2 observations as a function of the percent of the ICON's conjugate trace in sunlight.

when the ICON conjugate trace is in the darkness, suggesting that the excess when the sunlit conjugate is higher than 25% is due to CPE impact.

Since VERs from ICON measurements are determined assuming a homogeneous ionosphere, estimates when only part of the conjugate trace is sunlit might lead to miscalculations. Therefore, we only use measurements when the conjugate trace is completely illuminated (sunlit conjugate = 100%) to invert photoelectron energy spectra.

Photoelectron fluxes at selected altitudes are shown in Figure 3a for the same example as Figure 2. The fluxes were estimated by solving Equation 6 via RWLS and averaged over ± 15 km altitude for comparison with rocket measurements. One-sigma error bars at 349 km altitude are included in the figure. Unrealistic small error values can be seen at low energy levels, which are produced because only the ICON statistical uncertainties were propagated. Neither COSMIC2 nor NRL-MSISE-00 report uncertainties and they could not be included in the calculations.

The estimated photoelectron flux shown in Figure 3a decreases slightly with decreasing altitude until the peak emission height (~ 285 km). Below this point, the photoelectron flux drops rapidly. At 219 km the 20 eV photoelectron flux is one order of magnitude lower than the one at 285 km. The difference in the photoelectron flux above and below the peak height can be explained by their dominant processes. Below the peak height, the photoelectrons are rapidly losing their energy due to collisions with neutrals, whereas above the peak the amount of photoelectrons barely varies since there are few collisions.

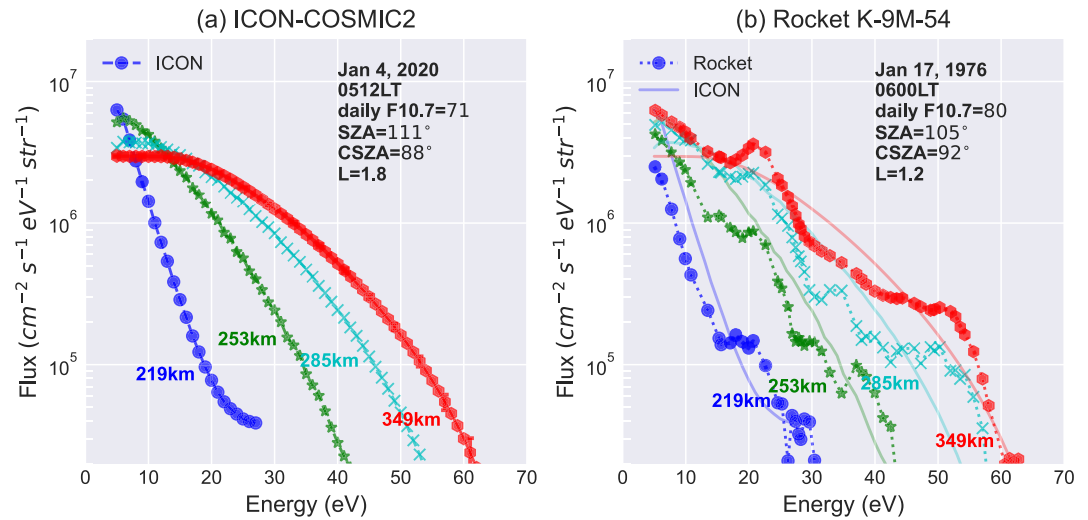


Figure 3. Photoelectron spectra at selected altitudes (a) Estimates using the proposed method at 31°N, 91°W on January 4, 2020 at 11:09 UTC, and (b) Measurements made on a rocket flight at Uchinoura, Japan (31°N, 131°E) on January 17, 1976 at 21:00 UTC. ICON fluxes from (a) are superimposed in (b).

6. Comparisons With Rocket Measurements

Measurements of the altitude variation of CPE fluxes are difficult to make, and therefore, are scarce. However (Mukai et al., 1979), made such measurements on a rocket flight (K-9M-54) in Japan on January 17, 1976 at solar minimum. These measurements were compared with FLIP model calculated fluxes by Richards and Peterson (2008), who reported a good agreement between model and data within the error bars, except for the 253 km spectrum. No explanation was provided for this discrepancy.

We compare the measured fluxes on January 17, 1976 with our ICON-COSMIC2 calculations on January 4, 2020 in Figure 3. This comparison is justified because photoelectron escape fluxes primarily depend on the solar EUV radiation, and the state of the plasmasphere and conjugate thermosphere. We verified that the day of year, solar flux index, and magnetic activity was similar for these two days. Although there is 4° difference in the conjugate solar zenith angle (CZSA) for the two experiments, escape fluxes are no sensitive to SZA when it is less than 95 (Lee et al., 1980; Richards & Peterson, 2008). The major difference in our comparison is the longer shell field line for ICON ($L = 1.8$), and the ICON conjugate point being in the high nighttime electron densities of the Weddell Sea Anomaly (Richards et al., 2017, 2018), which produces greater electron content along the ICON field line. There are also differences in the MSIS neutral densities, [O] was ~20% lower at 300 km for ICON.

For comparison purposes, we have superimposed the ICON and rocket fluxes in Figure 3b. Although the ICON spectra are smooth, their shape reproduces the rocket spectra very well at all altitudes. Interestingly, a reduced flux below <15 eV is observed for the ICON spectra at 349 km, which is most likely caused by the greater electron content along the ICON field line. Moreover, we observe that the ICON fluxes decrease more slowly with altitude than the rocket fluxes. This behavior is expected due to the lower neutral densities, and therefore, fewer collisions for ICON. FLIP model calculations not included here show a similar pattern.

7. Uncertainties

In this section, we discuss potential sources of uncertainties in our proposed method. They are: (a) the neutral atmosphere model; (b) the observing geometry and time resolution of FUV and RO measurements; (c) the derived average range $R(E)$, energy dissipation function $\lambda(E_k, z)$, and albedo-flux $A(E)$; and (d) the calibration factor of the ICON-FUV instrument.

While it is difficult to quantify the error introduced by the neutral atmosphere model, there is evidence that the NRL-MSISE00 model does not accurately reproduce the [O] density during solar minimum conditions (Meier

et al., 2015; Shepherd et al., 2016). In this work, the [O] density was scaled by a factor of 0.8 as suggested by Meier et al. (2015) to obtain the VER due to RR and MN.

Figure 2d shows that even when the conjugate trace is no sunlit (sunlit conjugate = 0–25%), the VER difference between ICON-FUV/COSMIC2 is not always zero. There is a small but consistent variance along time (~ 0.025). This variance is primarily attributed to the observing volume since the spatial and temporal resolution of ICON and COSMIC2 are not identical. The spatial resolution of ICON-FUV is $\sim 3^\circ$ in the horizontal direction and 0.093° in the vertical, compared to $\sim 12^\circ$ and 10° of COSMIC2. The time resolution of FUV and COSMIC2 is 12 s and 5–10 min, respectively. Such differences are important when the ionosphere is not horizontally homogeneous, for example, when observing the Equatorial Anomaly. From our data, Figure 2d, we calculated the maximum relative error introduced to the photoelectron flux estimation due to the geometric differences, which results in $0.025/0.25 = 10\%$.

Sergienko and Ivanov (1993) used a Monte-Carlo electron transport model to parametrize the electron range $R(E)$, the energy dissipation function $\lambda(E, z)$, and the albedo-flux $A(E)$ for mono-energetic electron and isotropic beams of energies > 50 eV. No measurements were done for energies below 50 eV. In this work, we have linearly extrapolated the values of R , λ , and A below 50 eV, which might introduce additional errors in the calculations. New measurements of R , λ , and A below 50 eV are required to accurately calculate photoelectron fluxes.

We used a factor of 0.5 to calibrate the ICON-FUV OI 135.6 nm measurements. Although comparisons of ICON-FUV products with COSMIC2, ISR, and GOLD suggest a similar value, the final calibration factor is still being validated and might differ from 0.5.

8. Summary and Conclusions

We presented a method for determining incoming photoelectron fluxes as a function of energy and altitude by combining global scale FUV and RO measurements. By using ICON-FUV and COSMIC-2 measurements, we demonstrated the capability of the proposed technique and examined its validity to characterize CPE spectra. Such characterization could provide important insight to the understanding of CPE, and its temporal and geographical distribution which will impact the ICON and future observations.

Through an extensive analysis of ICON-COSMIC2 conjunctions, we found a considerable amount of ICON-FUV nighttime measurements ($\sim 35\%$) affected by CPEs during the December solstice in the Northern hemisphere. The geographical and temporal distribution of measurements affected by CPEs closely coincides with that reported by Kil et al. (2020) using the SUSSI FUV instrument. Note that Kil et al. (2020) did not quantify the CPE contribution.

Finally, we compared our estimates with those made on a rocket flight in Japan. Despite the smooth spectra retrieved with our method, comparisons show a remarkable agreement in shape and magnitude at all altitudes. The major discrepancies are observed at energies < 15 eV and at lower altitudes, which are most likely explained by the greater electron content along the ICON field line and the lower MSIS neutral densities for ICON, respectively.

Data Availability Statement

Open research All ICON (FUV: L2.5 v4.0 r000), COSMIC2 (ionPrf: L2 v0001), and GOLD (Disk images: L1 v02 r01) data used in this work are available from <https://icon.ssl.berkeley.edu/Data>, <https://data.cosmic.ucar.edu/gnss-ro/cosmic2/provisional/spaceWeather/level2/>, and <https://gold.cs.ucf.edu/data/search/>; respectively.

References

- Anthes, R. A., & Schreiner, W. (2019). Six new satellites watch the atmosphere over Earth's equator. *Eos*, 100. <https://doi.org/10.1029/2019EO131779>
- Bailey, G. J., & Balan, N. (1996). A low-latitude ionosphere-plasmasphere model. In R. W. Schunk (Ed.), *Solar terrestrial energy program: Handbook on ionospheric models* (pp. 173–206). Utah State University.
- Banks, P. M., & Nagy, A. F. (1970). Concerning the influence of elastic scattering upon photoelectron transport and escape. *Journal of Geophysical Research*, 75(10), 1902–1910. <https://doi.org/10.1029/ja075i010p01902>
- Bennett, R. T. (1969). Latitude dependence of 6300 Å (OI) twilight airglow enhancement. *Journal of Geophysical Research*, 74(1), 381–383. <https://doi.org/10.1029/ja074i001p00381>
- Carlson, H. C. (1966). Ionospheric heating by magnetic conjugate-point photoelectrons. *Journal of Geophysical Research*, 71(1), 195–199. <https://doi.org/10.1029/jz071i001p00195>

Acknowledgments

This research was supported by NASA's Explorers Program under the Ionospheric CONnection Explorer (ICON) project contract number NNG12FA45C, and partially supported by NASA's grants NNG12FA42I, and 80NSSC20K0706 (JDH). The authors thank R. Meier for his helpful inputs and for providing computer-readable tables of electron impact excitation cross-sections. The authors also thank P. Richards for his valuable comments, and for providing experimental data and FLIP model calculations for validation of this work.

- Carlson, H. C. (1968). Most recent studies of low latitude effects due to conjugate location heating. *Radio Science*, 3(7), 668–673. <https://doi.org/10.1002/rds196837668>
- Carman, E. H., Hatzopoulos, G. J., & Heeran, M. P. (1969). Predawn enhancement of 6300 Å airglow in conjugate regions. *Planetary and Space Science*, 17(9), 1677–1679. [https://doi.org/10.1016/0032-0633\(69\)90155-x](https://doi.org/10.1016/0032-0633(69)90155-x)
- Christensen, A. B. (1975). Observations of OI 7774 emission excited by conjugate photoelectrons. *Planetary and Space Science*, 23(5), 831–842. [https://doi.org/10.1016/0032-0633\(75\)90020-3](https://doi.org/10.1016/0032-0633(75)90020-3)
- Christensen, A. B., Walterscheid, R. L., Ross, M. N., Meng, C.-I., Paxton, L. J., Anderson, D. E., Jr, et al. (1994). Global Ultraviolet Imager (GUVI) for the NASA Thermosphere-Ionosphere-Mesosphere Energetics and Dynamics (TIMED) mission. In J. Wang & P. B. Hays (Eds.), *Optical spectroscopic techniques and instrumentation for atmospheric and space research* (p. 451). <https://doi.org/10.1117/12.187583>
- Cogger, L. L., & Shepherd, G. G. (1969). Observations of a magnetic conjugate effect in the OI 6300 Å airglow at Saskatoon. *Planetary and Space Science*, 17(11), 1857–1865. [https://doi.org/10.1016/0032-0633\(69\)90160-3](https://doi.org/10.1016/0032-0633(69)90160-3)
- Cole, K. D. (1965). The predawn enhancement of 6300 Å airglow. *Annales Geophysicae*, 21(156), 196. <https://doi.org/10.1086/485789>
- Comberiate, J. M., Kamalabadi, F., & Paxton, L. J. (2007). A tomographic model for ionospheric imaging with the global ultraviolet imager. *Radio Science*, 42(2). <https://doi.org/10.1029/2005rs003348>
- Duboin, M. L., Lejeune, G., Petit, M., & Weill, G. (1968). Excitation of the oxygen lines and ionospheric heating by conjugate photoelectrons. *Journal of Atmospheric and Terrestrial Physics*, 30(2), 299–304. [https://doi.org/10.1016/0021-9169\(68\)90084-6](https://doi.org/10.1016/0021-9169(68)90084-6)
- Eastes, R. W., McClintock, W. E., Burns, A. G., Anderson, D. N., Andersson, L., Codrescu, M., et al. (2017). The Global-Scale Observations of the Limb and Disk (GOLD) Mission. *Space Science Reviews*, 212(1–2), 383–408. <https://doi.org/10.1007/s11214-017-0392-2>
- Eastes, R. W., McClintock, W. E., Codrescu, M. V., Aksnes, A., Anderson, D. N., Andersson, L., et al. (2008). Global-Scale Observations of the Limb and Disk (GOLD): New observing capabilities for the ionosphere-thermosphere. In *Geophysical Monograph Series* (Vol. 181, pp. 319–326). Blackwell Publishing Ltd. <https://doi.org/10.1029/181GM29>
- Evans, J. V. (1967). Midlatitude electron and ion temperatures at sunspot minimum. *Planetary and Space Science*, 15(10), 1557–1570. [https://doi.org/10.1016/0032-0633\(67\)90089-x](https://doi.org/10.1016/0032-0633(67)90089-x)
- Fontheim, E. G., Beutler, A. E., & Nagy, A. F. (1968). Theoretical calculations of the conjugate predawn effects. *Annales Geophysicae*, 24, 489.
- Hanson, W. B. (1963). Electron Temperatures in the Upper Atmosphere. *Space Research*, 3, 282. Retrieved from <https://ui.adsabs.harvard.edu/abs/1963spre.conf%2E282H/abstract>
- Hanson, W. B. (1969). Radiative recombination of atomic oxygen ions in the nighttime F region. *Journal of Geophysical Research*, 74(14), 3720–3722. <https://doi.org/10.1029/ja074i014p03720>
- Hanson, W. B. (1970). A comparison of the oxygen ion-ion neutralization and radiative recombination mechanisms for producing the ultraviolet nightglow. *Journal of Geophysical Research*, 75(22), 4343–4346. <https://doi.org/10.1029/ja075i022p04343>
- Immel, T. J., England, S. L., Mende, S. B., Heelis, R. A., Englert, C. R., Edelstein, J., et al. (2018). The Ionospheric Connection Explorer Mission: Mission Goals and Design. *Space Science Reviews*, 214(1), 13. <https://doi.org/10.1007/s11214-017-0449-2>
- Kaeppler, S. R., Sanchez, E., Varney, R. H., Irvin, R. J., Marshall, R. A., Bortnik, J., et al. (2020). Incoherent scatter radar observations of 10–100 keV precipitation: Review and outlook. In A. N. Jaynes, & M. E. Usanova (Eds.), *The dynamic loss of earth's radiation belts* (1st ed., Vol. 1, pp. 145–197). Elsevier. <https://doi.org/10.1016/B978-0-12-813371-2.00006-8>
- Kamalabadi, F., Qin, J., Harding, B. J., Iliou, D., Makela, J. J., Meier, R. R., et al. (2018). Inferring nighttime ionospheric parameters with the far ultraviolet imager onboard the ionospheric connection explorer. *Space Science Reviews*, 214(4), 70. <https://doi.org/10.1007/s11214-018-0502-9>
- Kil, H., Schaefer, R. K., Paxton, L. J., & Jee, G. (2020). The far ultraviolet signatures of conjugate photoelectrons seen by the special sensor ultraviolet spectrographic imager. *Geophysical Research Letters*, 47. <https://doi.org/10.1029/2019gl086383>
- Knudsen, W. C. (1970). Tropical ultraviolet nightglow from oxygen ion-ion neutralization. *Journal of Geophysical Research*, 75(19), 3862–3866. <https://doi.org/10.1029/ja075i019p03862>
- Kuo, Y., Wee, T., Sokolovskiy, S., Rocken, C., Schreiner, W., Hunt, D., & Anthes, R. A. (2004). Inversion and Error Estimation of GPS Radio Occultation Data. *Journal of the Meteorological Society of Japan*, 82(1B), 507–531. <https://doi.org/10.2151/jmsj.2004.507>
- Lee, J., Doering, J., Potemra, T., & Brace, L. (1980). Measurements of the ambient photoelectron spectrum from atmosphere explorer: I. AE-E measurements below 300 km during solar minimum conditions. *Planetary and Space Science*, 28(10), 947–971. [https://doi.org/10.1016/0032-0633\(80\)90058-6](https://doi.org/10.1016/0032-0633(80)90058-6)
- Lei, J., Syndergaard, S., Burns, A. G., Solomon, S. C., Wang, W., Zeng, Z., et al. (2007). Comparison of COSMIC ionospheric measurements with ground-based observations and model predictions: Preliminary results. *Journal of Geophysical Research*, 112. <https://doi.org/10.1029/2006JA012240>
- Meier, R. R. (1971). Observations of conjugate excitation of the O I 1304-A airglow. *Journal of Geophysical Research*, 76(1), 242–247. <https://doi.org/10.1029/ja076i001p00242>
- Meier, R. R. (1991). Ultraviolet spectroscopy and remote sensing of the upper atmosphere. *Space Science Reviews*, 58(1), 1–185. <https://doi.org/10.1007/BF01206000>
- Meier, R. R., Picone, J. M., Drob, D. P., Bishop, J., Emmert, J. T., Lean, J. L., et al. (2015). Remote Sensing of Earth's Limb by TIMED/GUVI: Retrieval of thermospheric composition and temperature. *Earth and Space Science*, 2(1), 1–37. <https://doi.org/10.1002/2014ea000035>
- Mende, S. B., Frey, H. U., Rider, K. A., Chou, C., Harris, S. E., Siegmund, O. H. W., et al. (2017). The far ultra-violet imager on the icon mission. *Space Science Reviews*, 212(1–2), 655–696. <https://doi.org/10.1007/s11214-017-0386-0>
- Molinaro, A. M., Simon, R., & Pfeiffer, R. M. (2005). Prediction error estimation: A comparison of resampling methods. *Bioinformatics*, 21(15), 3301–3307. <https://doi.org/10.1093/bioinformatics/bti499>
- Mukai, T., Kondo, Y., & Hiraoka, K. (1979). Rocket observation of conjugate photoelectrons in the predawn ionosphere. *Planetary and Space Science*, 27(1), 31–38. [https://doi.org/10.1016/0032-0633\(79\)90144-2](https://doi.org/10.1016/0032-0633(79)90144-2)
- Nagy, A. F., & Banks, P. M. (1970). Photoelectron fluxes in the ionosphere. *Journal of Geophysical Research*, 75(31), 6260–6270. <https://doi.org/10.1029/ja075i031p06260>
- Narasinga Rao, B. C., & Maier, E. J. R. (1970). Photoelectron flux and protonospheric heating during the conjugate point sunrise. *Journal of Geophysical Research*, 75(4), 816–822. <https://doi.org/10.1029/ja075i004p00816>
- Paxton, L. J., Schaefer, R. K., Zhang, Y., & Kil, H. (2017). Far ultraviolet instrument technology. *Journal of Geophysical Research: Space Physics*, 122, 2706–2733. <https://doi.org/10.1002/2016ja023578>
- Peterson, W. K., Doering, J. P., Potemra, T. A., McEntire, R. W., & Bostrom, C. O. (1977). Conjugate photoelectron fluxes observed on Atmosphere Explorer C. *Geophysical Research Letters*, 4(3), 109–112. <https://doi.org/10.1029/g1004i003p0109>
- Pfaff, R., Carlson, H. C., Watzin, J., Everrett, D., & Gruner, T. (2001). *An overview of the Fast Auroral Snapshot (FAST) satellite* [Vol. 98(1–2)]. Springer. https://doi.org/10.1007/978-94-010-0332-2_1

- Picone, J. M., Hedin, A. E., Drob, D. P., & Aikin, A. C. (2002). NRLMSISE-00 empirical model of the atmosphere: Statistical comparisons and scientific issues. *Journal of Geophysical Research*, *107*(A12), SIA 15-1–SIA 15-16. <https://doi.org/10.1029/2002JA009430>
- Qin, J., Makela, J. J., Kamalabadi, F., & Meier, R. R. (2015). Radiative transfer modeling of the OI 135.6 nm emission in the nighttime ionosphere. *Journal of Geophysical Research*, *120*, 10116–10135. <https://doi.org/10.1002/2015ja021687>
- Rees, M. (1963). Auroral ionization and excitation by incident energetic electrons. *Planet Space Science*, *11*, 1209–1218. [https://doi.org/10.1016/0032-0633\(63\)90252-6](https://doi.org/10.1016/0032-0633(63)90252-6)
- Rees, M. H., & Luckey, D. (1974). Auroral electron energy derived from ratio of spectroscopic emissions I. Model computations. *Journal of Geophysical Research*, *79*(34), 5181–5186. <https://doi.org/10.1029/ja079i034p05181>
- Richards, P. G., Meier, R. R., Chen, S., & Dandenault, P. (2018). Investigation of the Causes of the Longitudinal and Solar Cycle Variation of the Electron Density in the Bering Sea and Weddell Sea Anomalies. *Journal of Geophysical Research: Space Physics*, *123*, 7825–7842. <https://doi.org/10.1029/2018JA025413>
- Richards, P. G., Meier, R. R., Chen, S. S.-P., Drob, D. P., & Dandenault, P. (2017). Investigation of the causes of the longitudinal variation of the electron density in the Weddell Sea Anomaly. *Journal of Geophysical Research: Space Physics*, *122*, 6562–6583. <https://doi.org/10.1002/2016JA023565>
- Richards, P. G., & Peterson, W. K. (2008). Measured and modeled backscatter of ionospheric photoelectron fluxes. *Journal of Geophysical Research*, *113*, 1–13. <https://doi.org/10.1029/2008JA013092>
- Richards, P. G., & Torr, D. G. (1990). Auroral modeling of the 3371 Å emission rate: Dependence on characteristic electron energy. *Journal of Geophysical Research*, *95*(A7), 10337. <https://doi.org/10.1029/JA095iA07p10337>
- Schreiner, W., Rocken, C., Sokolovskiy, S., Syndergaard, S., & Hunt, D. (2007). Estimates of the precision of GPS radio occultations from the COSMIC/FORMOSAT-3 mission. *Geophysical Research Letters*, *34*, L04808. <https://doi.org/10.1029/2006gl027557>
- Schreiner, W. S., Sokolovskiy, S. V., Rocken, C., & Hunt, D. C. (1999). Analysis and validation of GPS/MET radio occultation data in the ionosphere. *Radio Science*, *34*(4), 949–966. <https://doi.org/10.1029/1999rs900034>
- Schreiner, W. S., Weiss, J. P., Anthes, R. A., Braun, J., Chu, V., Fong, J., et al. (2020). COSMIC-2 Radio Occultation Constellation: First Results. *Geophysical Research Letters*, *47*, 1–7. <https://doi.org/10.1029/2019GL086841>
- Semeter, J., & Kamalabadi, F. (2005). Determination of primary electron spectra from incoherent scatter radar measurements of the auroral E region. *Radio Science*, *40*(2). <https://doi.org/10.1029/2004rs003042>
- Sergienko, T., & Ivanov, V. (1993). A new approach to calculate the excitation of atmospheric gases by auroral electrons. *Annales Geophysicae*, *11*, 717–727.
- Shepherd, G. G., Cho, Y. M., Fomichev, V. I., & Martynenko, O. V. (2016). Thermospheric atomic oxygen concentrations from WINDII O+(2P-2D) 732 nm emission: Comparisons with the NRLMSISE-00 and C-IAM models and with GUVI observations. *Journal of Atmospheric and Solar-Terrestrial Physics*, *147*, 50–58. <https://doi.org/10.1016/j.jastp.2016.06.015>
- Shepherd, G. G., Pieau, J. F., Ogawa, T., Tohmatsu, T., Oyama, K., & Watanabe, Y. (1978). Direct measurement of conjugate photoelectrons and predawn 630 nm airglow. *Planetary and Space Science*, *26*(3), 211–217. [https://doi.org/10.1016/0032-0633\(78\)90086-7](https://doi.org/10.1016/0032-0633(78)90086-7)
- Simon-Wedlund, C., Lamy, H., Gustavsson, B., Sergienko, T., & Brändström, U. (2013). Estimating energy spectra of electron precipitation above auroral arcs from ground-based observations with radar and optics. *Journal of Geophysical Research: Space Physics*, *118*, 3672–3691. <https://doi.org/10.1002/jgra.50347>
- Smith, R. W. (1969). Some observations of the predawn enhancement of the red line airglow over Great Britain. *Planetary and Space Science*, *17*(5), 879–888. [https://doi.org/10.1016/0032-0633\(69\)90094-4](https://doi.org/10.1016/0032-0633(69)90094-4)
- Solomon, S. C. (2001). Auroral particle transport using Monte Carlo and hybrid methods. *Journal of Geophysical Research*, *106*(No. A1), 107–116. <https://doi.org/10.1029/2000JA002011>
- Solomon, S. C. (2017). Global modeling of thermospheric airglow in the far ultraviolet. *Journal of Geophysical Research: Space Physics*, *122*(7), 7834–7848. <https://doi.org/10.1002/2017JA024314>
- Solomon, S. C., Andersson, L., Burns, A. G., Eastes, R. W., Martinis, C., McClintock, W. E., & Richmond, A. D. (2020). Global-Scale Observations and Modeling of Far-Ultraviolet Airglow During Twilight. *Journal of Geophysical Research: Space Physics*, *125*. <https://doi.org/10.1029/2019JA027645>
- Stolarski, R. S. (1968). Calculation of auroral emission rates and heating effects. *Planetary and Space Science*, *16*(10), 1265–1276. [https://doi.org/10.1016/0032-0633\(68\)90031-7](https://doi.org/10.1016/0032-0633(68)90031-7)
- Strickland, D. J., Meier, R. R., Hecht, J. H., Christensen, A. B., Strickland, D. J., & Meier, R. R. (1989). Deducing composition and incident electron spectra from ground-based auroral optical measurements: Variations in oxygen density. *Journal of Geophysical Research*, *94*(A10), 13553. <https://doi.org/10.1029/JA094iA10p13553>
- Swartz, W. E. (1972). *Electron production, recombination and heating in the F region of the ionosphere (Doctoral dissertation)*. The Pennsylvania University. Retrieved from <https://www.proquest.com/docview/302671735>
- Syndergaard, S., Kursinski, E. R., Herman, B. M., Lane, E. M., & Flittner, D. E. (2005). A refractive index mapping operator for assimilation of occultation data. *Monthly Weather Review*, *133*(9), 2650–2668. <https://doi.org/10.1175/MWR3001.1>
- Tien, J., Okiihiro, B. B., Esterhuizen, S., Franklin, G., Meehan, T., Munson, T., et al. (2012). Next Generation Scalable Spaceborne GNSS Science Receiver. In *Proceedings of the 2012 international technical meeting of the institute of navigation* (pp. 882–914). Retrieved from <http://www.ion.org/publications/abstract.cfm?ip=p&articleID=9999>
- Tinsley, B. A., Christensen, A. B., Bittencourt, J., Gouveia, H., Anreji, P. D., & Takahashi, H. (1973). Excitation of oxygen permitted line emissions in the tropical nightglow. *Journal of Geophysical Research*, *78*(7), 1174–1186. <https://doi.org/10.1029/ja078i007p01174>
- Varney, R. H., Swartz, W. E., Hysell, D. L., & Huba, J. D. (2012). SAMI2-PE: A model of the ionosphere including multistream interhemispheric photoelectron transport. *Journal of Geophysical Research*, *117*(A6). <https://doi.org/10.1029/2011JA017280>
- Wautelet, G., Hubert, B., Gérard, J.-C., Immel, T. J., Frey, H. U., Mende, S. B., et al. (2021). First ICON-FUV nighttime NmF2 and hmF2 comparison to ground and space-based measurements. *Journal of Geophysical Research: Space Physics*, *126*, e2021JA029360. <https://doi.org/10.1029/2021JA029360>
- Yue, X., Schreiner, W. S., Kuo, Y. H., Hunt, D. C., & Rocken, C. (2013). GNSS radio occultation technique and space weather monitoring. *26th international technical meeting of the satellite Division of the institute of navigation, ION GNSS 2013*, 3(September 2013), 2508–2522.
- Yue, X., Schreiner, W. S., Pedatella, N., Anthes, R. A., Mannucci, A. J., Straus, P. R., & Liu, J.-Y. (2014). Space Weather Observations by GNSS Radio Occultation: From FORMOSAT-3/COSMIC to FORMOSAT-7/COSMIC-2. *Space Weather*, *12*(11), 616–621. <https://doi.org/10.1002/2014sw001133>
- Zhang, B., Makram-Ebeid, S., Prevost, R., & Pizaine, G. (2014). Fast solver for some computational imaging problems: A regularized weighted least-squares approach. *Digital Signal Processing*, *27*, 107–118. <https://doi.org/10.1016/j.dsp.2014.01.007>